Rebound Relays and Inhibitory Vetoes Stabilize Sparse Sequential Activity in HVC

Zeina Bou Diab[1], Arij Daou[1*]

1. Neurophysiology and Computational Neuroscience Group, Biomedical Engineering Program, American University of Beirut, Lebanon

* Corresponding author: arij.daou@aub.edu.lb

Abstract

Brains build behavior by chaining actions and perceptions into precisely timed sequences, an ability central to speech, skilled movement, and memory, yet the circuit logic that propagates sequences remains unclear. Songbird HVC captures this problem: premotor HVC_{RA} neurons burst once per motif, while basal ganglia-projecting HVC_X neurons burst 2-4 times across the same motif. We developed a biophysically grounded HVC network as linked microcircuits encoding sub-syllabic segments. The model highlights inhibition not merely as suppressive but actively structuring sequence propagation and fidelity. Tonic inhibitory epochs prime HVC_X by deinactivating T-type Ca^{2+} channels and recruiting I_h, so that release elicits precisely timed rebound bursts that recruit the next HVC_{RA} ensemble. A complementary phasic inhibitory veto suppresses off-time activation, preventing pathological restarts while preserving HVC_{RA} single-burst sparseness. More broadly, inhibitory timing can serve as the brain's internal "clocked handshake," converting suppression into forward drive to advance sequences while enforcing error-corrected precision.

Introduction

The ability to learn and generate ordered patterns of activity is a cornerstone of cognition and behavior. Across systems - navigation, decision making, and skilled movement - neural populations represent time not as a static variable but as structured trajectories that enable prediction, planning, and action[1–6]. Yet a mechanistic question remains central: how do circuits propagate precise sequences while preventing spurious reactivation and preserving cell-type specific firing patterns?

Songbird vocal behavior provides a canonical model for addressing this question in a learned sensorimotor sequence. Birds acquire song through iterative practice guided by auditory feedback, and adulthood retains flexibility for ongoing maintenance and modification. This learning is supported by a well-defined circuit architecture comprising a vocal motor pathway and a cortico-basal ganglia loop (Figure 1 in Bou Diab et al[7]), enabling unusually direct links between circuit dynamics, behavioral output, and plasticity. At the core of this system lies HVC, a telencephalic nucleus often considered homologous to mammalian cortical layer III[8,9]. HVC functions as a pattern generator and "conductor" of song, encoding syllable order and fine temporal structure through stereotyped commands that ultimately drive vocal and respiratory musculature[10–15].

HVC is mechanistically tractable because it comprises a small set of principal cell classes with distinct connectivity and firing regimes. HVC_{RA} neurons provide timing signals to the robust nucleus of the arcopallium (RA) and downstream motor centers[14,16], while HVC_{X} neurons project to basal ganglia Area X, linking sequence generation to reinforcement-driven learning[17]. Local fast-spiking interneurons (HVC_{INT}) densely regulate both projection classes, shaping timing and reliability of activity. *In vivo*, this division is reflected

in strikingly different spike patterns: during singing, HVC_{RA} neurons fire a single brief burst (~10 ms) locked to a specific moment in the motif[18,19], HVC_X neurons generate multiple bursts (2-4) that are likewise stereotyped and motor-locked[19,20], and HVC_{INT} neurons exhibit sustained firing with structured epochs of bursting and suppression[18,19,21–25]. Recent reanalysis further suggests that HVC_X bursting may form multiple concurrent motif-spanning sequences ("parallel lines"), pointing to a richer temporal code in HVC_X than previously appreciated[26,27].

Decades of intracellular work constrain the intrinsic and synaptic mechanisms available to produce these patterns. *In vitro* and *in vivo* recordings demonstrate that HVC_{RA}, HVC_X, and HVC_{INT} exhibit distinct electrophysiological signatures shaped by specific complements of ion channels[28–34]. Paired recordings in slices revealed a core microcircuit motif: projection neurons excite interneurons, interneurons inhibit both projection classes, with evidence for monosynaptic excitation from HVC_X to HVC_{RA} embedded in a larger landscape of disynaptic inhibition[24,32]. Multiple computational models have been proposed for HVC sequence generation, invoking intrinsic chaining, extrinsic feedback, or both[7,13,23,25,35–42]. Yet most do not simultaneously capture realistic spike morphology with biophysical currents, include all major HVC classes, and reproduce the distinct in vivo firing patterns across populations; even recent biophysically grounded microcircuit models leave open how HVC_X and interneurons causally advance sequences and generate motif-spanning HVC_X structure[7,27].

Recent causal and synaptic-mapping work has sharpened key constraints. Trusel et al.[43] showed that once song is initiated, HVC can sustain progression through the learned motif largely independent of major extrinsic input pathways, and that brief excitation within

HVC can trigger “skipping record”-like restarts that rely on local circuitry. Importantly, their connectivity mapping finds HVC_X neurons consistently making monosynaptic connections onto HVC_{RA} neurons, but only very sparsely onto other HVC_X neurons, supporting a sequence-generating network built around heterotypic excitation between the two projection classes. These results elevate HVC_X from a corollary channel for basal ganglia learning to a potential causal relay within the premotor pattern generator itself.

Here we present a biophysically grounded model of HVC that reframes sequence generation around that relay. The model organizes HVC as a chain of linked microcircuits encoding sub-syllabic segments and integrates experimentally constrained synaptic architecture with realistic intrinsic currents. We show how tonic inhibition primes HVC_X neurons for post-inhibitory rebound via T-type Ca^{2+} deinactivation and I_h recruitment, so that release generates precisely timed bursts that recruit the next HVC_{RA} ensemble, while a complementary phasic inhibitory veto suppresses off-time reactivation to preserve HVC_{RA} single-burst sparseness. This framework links defined cellular conductances to motif-scale sequence integrity and yields concrete, testable predictions for how manipulating GABAergic tone or HVC_X intrinsic currents should reshape propagation, burst multiplicity, and timing.

Results

Zebra finch song is an exceptionally precise learned sequence: each motif comprises stereotyped syllables produced with millisecond timing across renditions. In HVC, this precision is expressed as distinct population codes; HVC_{RA} neurons emit a single brief burst per motif time point, HVC_X neurons generate multiple motif-locked bursts, and local interneurons fire densely with structured epochs of activation and suppression. Dominant synaptic motifs and key intrinsic conductances have been characterized across these classes[24,32,34,44], providing unusually strong constraints for mechanistic modeling.

Here we build a biophysically grounded HVC network to ask what circuit mechanisms are sufficient to propagate a sparse sequence with HVC_{RA} single-burst precision while preserving multi-burst HVC_X dynamics and realistic interneuron activity. We first define a microcircuit-chain architecture (Figure 1), then show how propagation is carried by an HVC_X-mediated relay that converts inhibition into forward drive, while complementary inhibition suppresses spurious HVC_{RA} reactivation. Finally, we map parameter regimes that stabilize propagation and predict perturbations that fragment the sequence, change HVC_X burst multiplicity, or warp motif timing.

Network Architecture: HVC_X to HVC_{RA} driven activity

We modeled HVC as a chain of repeating microcircuits arranged in a functional chain, each representing the minimal unit required to generate activity for a sub-syllabic segment (SSS)[7]. A motif composed of *N* SSSs is implemented as *N* linked microcircuits, each recruiting a dedicated ensemble whose coordinated intrinsic and synaptic dynamics both encode the local segment and advance activity to the next. This framing converts the core

problem of song timing into a mechanistic one: identify the minimal, biophysically grounded circuit ingredients that can propagate a sparse sequence while preserving the distinct firing regimes of HVC_{RA}, HVC_X, and interneurons.

Structural organization of the network

Figure 1 summarizes the network architecture and population structure. The model contains a total pool of 120 HVC_{RA} neurons (red), 60 HVC_X neurons (light/dark blue), and 60 interneurons split into 20 phasic-bursting interneurons (INT_{PB}) (green) and 40 tonic-bursting interneurons (INT_{TB}) (light/dark black), preserving the reported 2:1:1 proportionality across HVC_{RA}: HVC_{INT}: HVC_X [31,44]. For computational tractability, we instantiated 20 microcircuits (i.e., 20 SSSs); both the number of microcircuits and absolute population sizes are scalable without changing the architectural logic. We use two operational interneuron classes to capture the inhibitory motifs required for realistic output: PB interneurons produce a single, time-locked burst, whereas TB interneurons generate multiple bursts across the motif. As shown below, these modes play complementary roles in propagation and in preventing spurious sequence reactivation.

Each microcircuit (gray oval) contains a **microcircuit-specific** (MS) HVC_{RA} ensemble - a random group of HVC_{RA} neurons drawn from the global pool (ensemble size chosen randomly; see below) - and exactly three MS control neurons: one INT_{PB}, one INT_{TB}, and one MS HVC_X neuron (X_{SSS}). “Microcircuit-specific” denotes neurons that belong to one and only one microcircuit and are required for robust sequential propagation. All remaining interneurons and HVC_X neurons are non-microcircuit-specific (NMS), and can receive/deliver synapses broadly (subject to pre/post cell-type rules), providing a

distributed inhibitory-excitatory background that interacts with microcircuit dynamics (Figure 1).

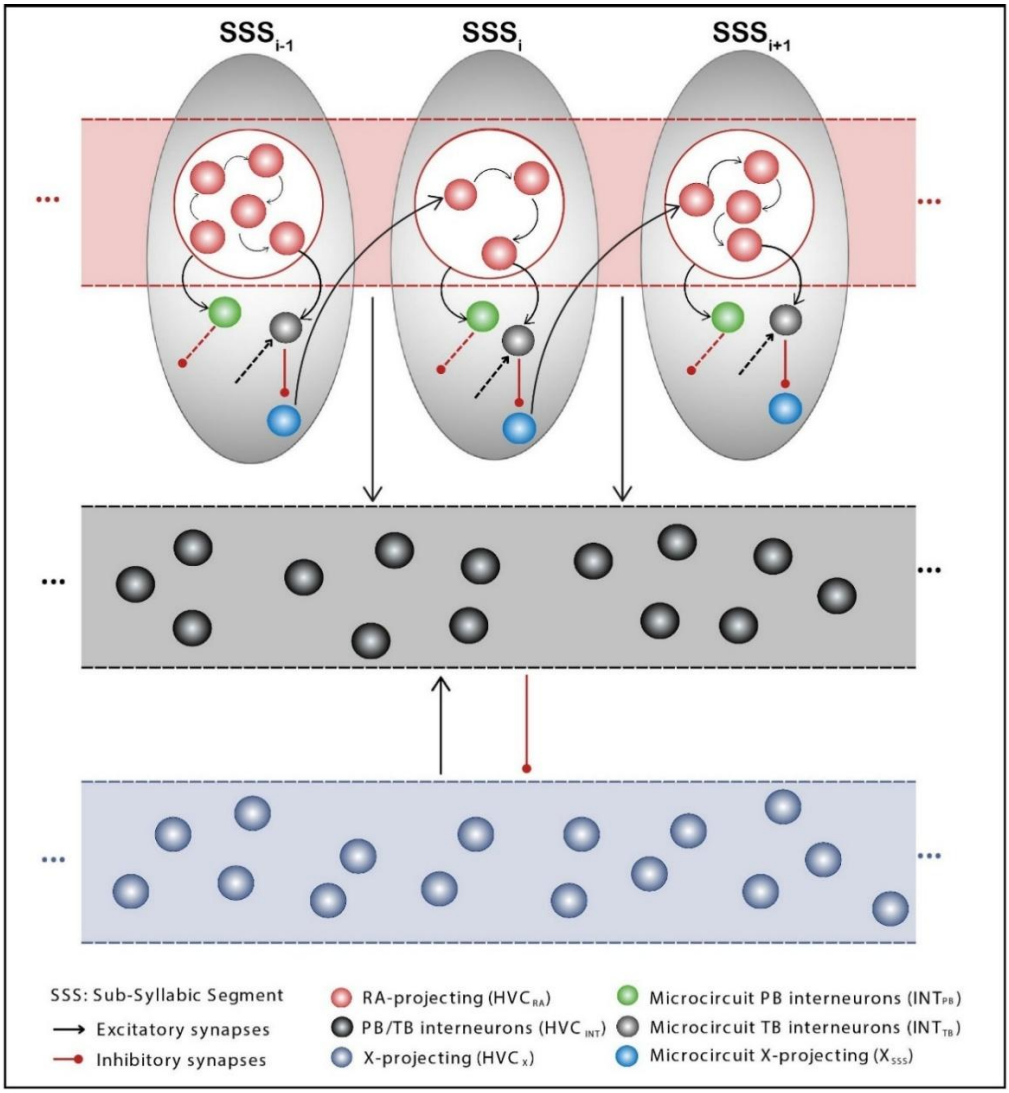

Figure 1. Microcircuit-chain architecture of the HVC network model. HVC is modeled as a chain of repeating microcircuits, each corresponding to one sub-syllabic segment (SSS) of the motif (illustrated for SSS_{i-1}, SSS_i, and SSS_{i+1}). Within each microcircuit (gray oval), a small ensemble of RA-projecting neurons (HVC_{RA}; red) is connected by directed AMPAergic links (black arrows) and recruits three microcircuit-specific elements: a phasic-bursting interneuron (INT_{PB}; green), a tonic-bursting interneuron (INT_{TB}; gray), and a microcircuit-specific X-projecting neuron (X_{SSS}; dark blue). HVC_{RA} activity drives local inhibition; INT_{TB} inhibits X_{SSS}, which then provides excitatory drive to the first HVC_{RA} neuron of the next microcircuit, implementing segment-to-segment propagation. Microcircuits are embedded within global pools of non-microcircuit-specific interneurons (PB/TB HVC_{INT}; emphasized black zone) and HVC_X neurons (emphasized blue zone) that interact sparsely and reciprocally, providing distributed background coupling across segments. Black arrows denote excitatory synapses and red symbols denote inhibitory synapses; ellipses indicate repetition across the motif.

Synaptic connectivity in the network

To translate the microcircuit-chain hypothesis into a mechanistic network, we implemented a connectivity scheme that is minimal, cell-type grounded, and explicitly designed to separate three functions: (i) generate a brief, sparse HVC_{RA} burst packet within each microcircuit, (ii) recruit precisely timed inhibition that shapes burst termination and de-inactivation dynamics, and (iii) transmit activity forward to the next microcircuit through an HVC_X-mediated relay.

Feedforward HVC_{RA} chaining within each microcircuit. The 120 HVC_{RA} neurons are partitioned across 20 microcircuits, with each microcircuit recruiting a random HVC_{RA} ensemble of 3-10 neurons. Within microcircuit i, these neurons are ordered into a directed AMPAergic chain: $HVC^i_{RA_1} \rightarrow HVC^i_{RA_2} \rightarrow \ldots HVC^i_{RA_m}$ (Figure 1). This implementation enforces a key constraint of the song system: local excitation is temporally ordered, providing a transparent substrate for generating a brief, temporally ordered HVC_{RA} packet.

Microcircuit-specific inhibition splits into phasic and tonic control. Each microcircuit contains two inhibitory controllers with distinct targets and roles. All HVC_{RA} neurons in microcircuit i excite INT^i_{PB} via AMPA synapses, making INT^i_{PB} a rapid readout of microcircuit activation positioned to deliver precisely timed inhibition that prevents unwanted reverberation (mechanism dissected below). In contrast, only the terminal HVC_{RA} neuron ($HVC^i_{RA_m}$) excites INT^i_{TB}, implementing an "end-of-segment" signal that couples TB recruitment to microcircuit completion. In addition, each INT^i_{TB} can receive excitation from a random subset of HVC_{RA} and HVC_X neurons across the network, and each INT^i_{PB} can inhibit selected HVC_{RA} or HVC_X (Figure 1).

HVCX relay converts inhibition into forward drive. INT_{TB}^{i} inhibits the MS HVCX neuron X_{SSS}^{i} via GABAergic synapses. Critically, X_{SSS}^{i} then excites the first HVCRA neuron of the next microcircuit, $HVC_{RA_1}^{i+1}$, via an AMPA synapse. This single motif - HVCRA chain → TB inhibition → HVCX rebound → next HVCRA chain - is the backbone of propagation in the model, and is consistent with recent evidence for robust HVCX → HVCRA connectivity[43].

Distributed NMS coupling. To introduce realistic background interactions without hardwiring additional sequence structure, we included sparse probabilistic coupling through NMS pools. HVCRA neurons provide random AMPA excitation to NMS interneurons (each HVCRA contacting 1-3 randomly chosen NMS interneurons). NMS interneurons inhibit NMS HVCX neurons (1-3 targets per interneuron), and NMS HVCX neurons reciprocally excite NMS interneurons (1-3 targets per HVCX). These low-density interactions supply a distributed inhibitory-excitatory backdrop while keeping sequence propagation primarily determined by the microcircuit relay.

Functional connectivity implements propagation while enforcing cell-type specific firing regimes. Figure 2 summarizes how the model's two inhibitory modes - phasic and tonic bursting interneurons - coordinate with HVCRA and HVCX neurons to propagate activity across sub-syllabic segments (SSSs) while preserving each class's *in vivo*-like firing regime. Traces are shown for four example microcircuits (gray boxes): two consecutive segments (microcircuits i and $i+1$, encoding SSS_i and SSS_{i+1}) and two later, nonconsecutive microcircuits (j and k, encoding SSS_j and SSS_k). Each microcircuit recruits a randomly sized HVCRA ensemble (here 5, 3, 6, and 7 neurons, respectively), reflecting stochastic assignment of 3-10 HVCRA neurons per microcircuit.

HVC_{RA} packets define local segments; PB interneurons define the segment "window". Within each microcircuit, sequential HVC_{RA} bursting is generated by directed AMPA coupling along the local HVC_{RA} chain (Figure 1), producing a brief, ordered packet aligned to that SSS. Because all HVC_{RA} neurons in a microcircuit excite its MS phasic interneuron (INT_{PB}), INT_{PB} integrates the HVC_{RA} packet and produces a segment-spanning inhibitory burst. For example, in microcircuit i, the five HVC_{RA} neurons collectively drive INT_{TB}^{i}, generating a "long" phasic burst whose onset coincides with the first spike of $HVC_{RA_1}^{i}$ and whose offset tracks the last spike of $HVC_{RA_5}^{i}$, thereby defining the temporal window of SSS_i (Figure 2, green trace under SSS_i). Functionally, this "windowing" role resembles feedforward inhibition in cortical circuits, where rapidly recruited interneurons impose a narrow time window for excitation to influence spiking and suppress late destabilizing drive[45,46]. In this sense, INT_{PB} structures time rather than simply suppressing activity.

TB interneurons mark segment completion and recruit HVC_X rebound bursting to propagate forward. In contrast, the MS tonic interneuron (INT_{TB}) is driven primarily by the terminal HVC_{RA} neuron of the local chain. In microcircuit i, $HVC_{RA_m}^{i}$ excites INT_{TB}^{i}, producing a burst near the end of SSS_i. INT_{TB}^{i} then inhibits the MS X-projecting neuron X_{SSS}^{i}, producing a pronounced hyperpolarizing "sag" in X_{SSS}^{i} (Figure 2, blue). Release from this inhibition triggers a rebound burst in X_{SSS}^{i}, which excites the first HVC_{RA} neuron of the next microcircuit, $HVC_{RA_1}^{i+1}$, initiating the HVC_{RA} chain for SSS_{i+1}. Thus, the backbone of propagation is: tonic inhibition → HVC_X rebound → next-segment HVC_{RA} recruitment, a conserved computational motif in which inhibition becomes a precisely timed trigger[47–49].

This logic then repeats across microcircuits (INT_{PB}^{i+1} spans SSS_{i+1}; INT_{TB}^{i+1} recruits rebound in X_{SSS}^{i+1}; activity advances to microcircuit $i+2$).

Why two inhibitory modes are required: preventing restarts while allowing multi-burst HVCX. A key challenge is that the same relay that advances the sequence ($X_{SSS}^{i} \rightarrow HVC_{RA_1}^{i+1}$) also creates vulnerability to spurious reactivation if X_{SSS}^{i} rebounds multiple times. In the model, INT_{TB}^{i} can be recruited not only by the terminal HVCRA neuron in microcircuit i, but also by excitatory inputs from HVCRA and HVCX neurons in other microcircuits. In the example shown, INT_{TB}^{i} receives additional excitation from $HVC_{RA_2}^{j}$, $HVC_{RA_2}^{k}$ and $HVC_{RA_5}^{k}$, producing four tonic bursts across the motif (Figure 2, black trace), each inducing a corresponding inhibition-and-release event in X_{SSS}^{i} and thus multiple rebound bursts (Figure 2, blue). This naturally yields the experimentally observed multi-burst regime of HVCX neurons (2-4 bursts per motif). Without additional control, each rebound burst would re-excite $HVC_{RA_1}^{i+1}$ and re-trigger the HVCRA chain in microcircuit $i+1$, producing extra HVCRA bursts that violate the hallmark single-burst regime and effectively mimic pathological "restart-like" dynamics. The model prevents this failure mode through the phasic inhibitory gate: for any segment SSS_x, INT_{PB}^{x} suppresses HVCRA neurons attempting to fire outside their assigned window. Accordingly, the "extra" X_{SSS}^{i} rebounds that occur during later segments (SSS_j and SSS_k) are vetoed by INT_{PB}^{j} and INT_{PB}^{k}, which silence $HVC_{RA_1}^{i+1}$ at those inappropriate times (Figure 2, red), preventing unwanted reactivation of microcircuit $i+1$.

Together, these mechanisms assign complementary roles to inhibition: tonic inhibition recruits rebound bursting in HVCX to provide a reliable forward-propagating trigger,

whereas phasic inhibition enforces temporal exclusivity so that only the HVC_{RA} ensemble assigned to an SSS, bursts during that SSS. This division of labor reconciles multi-burst HVC_X with single-burst HVC_{RA} within a single propagating sequence and mirrors stabilization strategies in other sequence-generating circuits, where progression depends on release-from-inhibition while parallel inhibitory motifs prevent re-entrant dynamics[50,51].

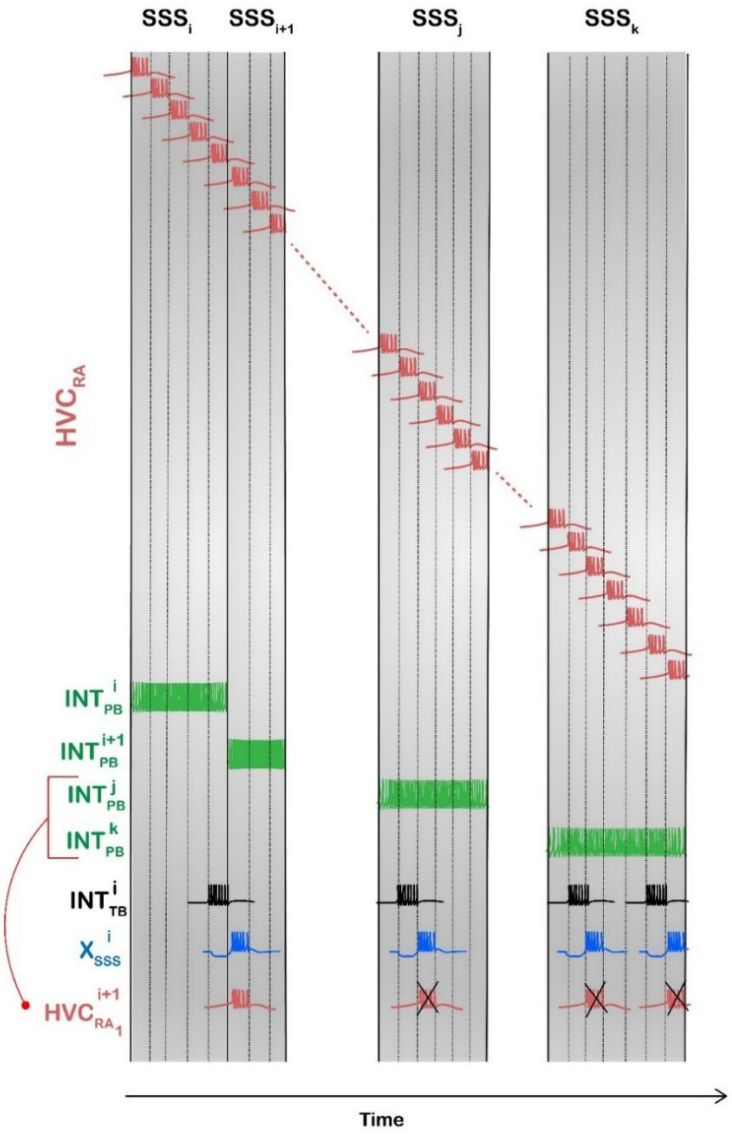

Figure 2. Functional logic for propagation and stability in the microcircuit chain. Representative membrane potential traces showing how microcircuit-specific phasic and tonic inhibition coordinates HVC_{RA} and HVC_X activity to advance the sequence while preventing spurious reactivation. Gray boxes depict four sub-syllabic segments (SSSs): two consecutive microcircuits (SSS_i and SSS_{i+1}) and two later, nonconsecutive segments (SSS_j and SSS_k). Top (**red**):

within each SSS, a randomly sized HVC_{RA} ensemble (examples: 5, 3, 6, 7 cells) generates an ordered burst packet via feedforward AMPA chaining. **Green**: the MS phasic interneuron INT_{PB} integrates excitation from the local HVC_{RA} ensemble and produces a segment-spanning inhibitory epoch that defines the SSS temporal "window." **Black:** at segment completion, the tonic interneuron (INT_{TB}^{i}) inhibits the MS X-projector (X_{SSS}^{i}, **blue**), producing a hyperpolarizing sag; release triggers a rebound burst that excites the first HVC_{RA} neuron of the next microcircuit ($HVC_{RA_1}^{i+1}$, **red**) to initiate the next packet. Additional tonic bursts (driven by later-segment excitation) generate extra X_{SSS}^{i} rebounds; phasic inhibition from the active segment (INT_{PB}^{j}, INT_{PB}^{k}) vetoes the resulting out-of-window activations of $HVC_{RA_1}^{i+1}$ (X marks), preventing pathological restarts while preserving single-burst HVC_{RA} alongside multi-burst HVC_X. Time runs left to right.

Activity patterns of HVC_{RA} neurons

We first describe the population activity produced by the network (Figures 3-5). HVC_{RA} neurons burst with extreme sparsity, generating at most one burst per motif (typically 4-6 spikes). Across simulations, HVC_{RA} bursts lasted 7.94 ± 0.92 ms and contained 5.89 ± 0.74 spikes, reproducing the defining *in vivo* signature of HVC_{RA} during singing - brief, precisely time-locked bursting with a single event per motif time point[19,52]. Figure 3 visualizes this sparse code for 30 HVC_{RA} neurons aligned to a representative syllable segmented into five sub-syllabic segments (SSS_i - SSS_{i+4}). Consistent with the random recruitment rule (3-10 HVC_{RA} neurons per microcircuit), the number of HVC_{RA} neurons assigned to each segment varies (here: 5, 3, 4, 12, and 6, respectively; vertical boundaries). Within each microcircuit, ordered HVC_{RA} bursting arises from feedforward excitation along the local HVC_{RA} chain (Figure 1), producing a compact packet confined to the segment window.

Notably, the first HVC_{RA} neuron in each microcircuit exhibits small subthreshold "bumps," reflecting excitatory drive from the corresponding microcircuit-specific HVC_X neuron. Because each X_{SSS} generates 2-4 rebound bursts (Figure 2), the first rebound burst providing the forward-propagating trigger to the next microcircuit and later bursts reflecting additional inhibition-release events from INT_{TB}, these HVC_X-driven depolarizations would, in principle, create unwanted HVC_{RA} reactivations and restart the

local chain outside its assigned segment. In the model, these incipient events are vetoed by phasic inhibition: the segment-appropriate INT_{PB} suppresses HVCRA spiking at off-time moments. For example, $HVC_{RA_1}^{i}$ shows three bumps during SSS_{i+2} - SSS_{i+4} because upstream X_{SSS}^{i-1} rebounds during those later segments, but spiking is silenced by INT_{PB}^{i+2}, INT_{PB}^{i+3} and INT_{PB}^{i+4}. We dissect this inhibitory veto mechanism directly in Figure 6.

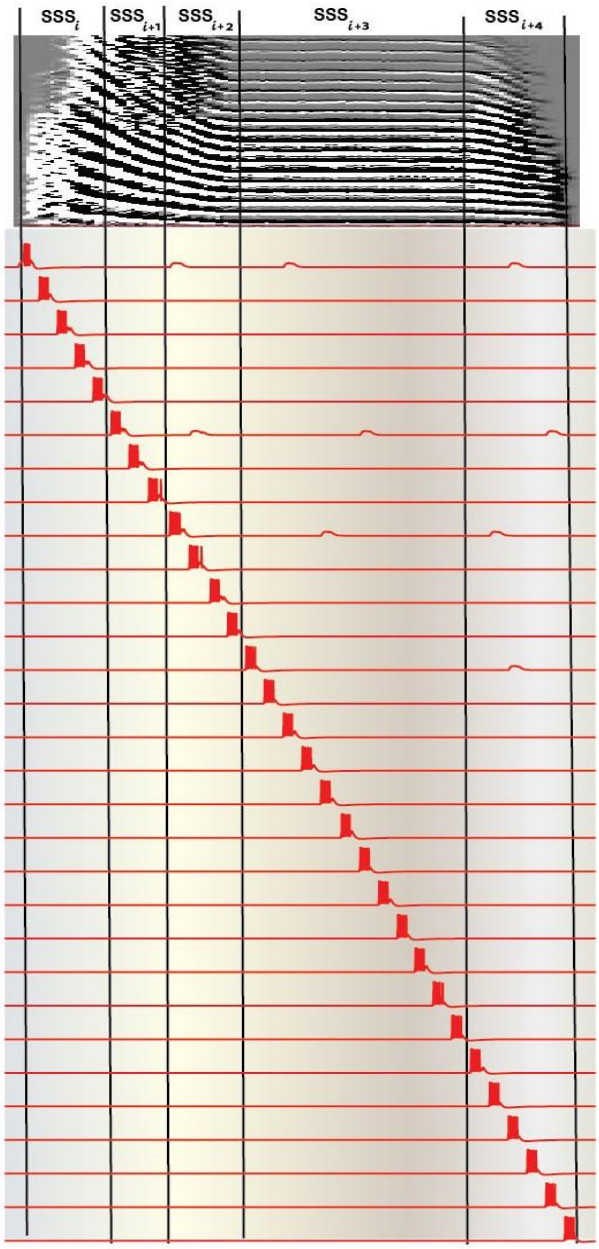

Figure 3. Ultra-sparse, segment-locked HVC_{RA} bursting in the model. Top: Example syllable waveform partitioned into five sub-syllabic segments (SSS_i - SSS_{i+4}; boundaries indicated by vertical lines). **Bottom**: Membrane potential traces from 30 representative HVC_{RA} neurons aligned to the syllable. HVC_{RA} neurons emit at most one brief burst per motif (typically 4-6 spikes), with different neurons bursting at distinct times to form a sparse sequential packet. Differences in burst density across SSSs reflect random recruitment of 3-10 HVC_{RA} neurons per microcircuit. Subthreshold depolarizations ("bumps"), most prominent in chain-initiating HVC_{RA} neurons, arise from excitatory input driven by microcircuit-specific HVC_X rebound bursts; segment-specific phasic inhibition vetoes these inputs to prevent off-time HVC_{RA} reactivation (Figure 6).

Determinants of HVC_{RA} burst strength, spike count, onset timing, and propagation robustness. Beyond enforcing sparsity, the model specifies how each HVC_{RA} burst - its onset latency, spike count, and duration - emerges from a constrained interaction between synaptic drive and intrinsic excitability, and shows that the same "control knobs" that tune burst shape also define the boundary between stable propagation and sequence failure. First, burst strength and onset latency are set by the effective AMPA conductance recruiting each HVC_{RA} neuron: either $HVC_{RA} \rightarrow HVC_{RA}$ within a microcircuit (for non-initial chain elements) or $X_{SSS}^{i} \rightarrow HVC_{RA_1}^{i+1}$ across the microcircuit boundary (for the chain-initiating neuron). In both cases, larger g_{AMPA} yields stronger bursts, more spikes, and shorter first-spike delays, consistent with synaptic control of recruitment timing in feedforward sequences. Second, spike onset and burst size are shaped intrinsically by the A-type K^+ conductance (g_A): increasing g_A delays recruitment and reduces spike count by lowering effective excitability. Third, burst termination is governed by the Ca^{2+}-dependent K^+ conductance (g_{SK}): Ca^{2+}entry through the L-type current (I_{CaL}) accumulates during the burst, progressively recruiting I_{SK} until the outward current curtails spiking[7]. Together, these mechanisms give a biophysical account of why HVC_{RA} bursts remain brief and stereotyped while still being tunable by synaptic drive and intrinsic conductance state.

Crucially, proper sequence propagation is not guaranteed by architecture alone: it requires that these parameters remain within a bounded regime. Supplementary Figure 2 identifies three HVC_{RA}-level failure modes that fracture propagation. First, within-microcircuit chaining fails if the AMPA conductance between successive HVC_{RA} neurons is sufficiently small that postsynaptic neurons cannot reach threshold. Second, propagation fails at microcircuit boundaries if $X_{SSS}^{i} \rightarrow HVC_{RA_1}^{i+1}$ AMPA drive is too weak to recruit the next chain's initiator (Supplementary Figure 2A). Third, even with intact synaptic connectivity, propagation can be eliminated when intrinsic "braking" currents push HVC_{RA} neurons outside a burst-permissive excitability regime: sufficiently large g_A or g_{SK} can abolish bursting altogether (Supplementary Figure 2B-C). Thus, robust HVC_{RA} propagation requires a minimum synaptic gain (both within-chain and X → HVC_{RA} coupling and a bounded intrinsic "braking" regime (particularly g_A and g_{SK}).

Activity patterns of HVC_{INT} neurons and tonic-interneuron failure modes that destabilize propagation. Tonic-bursting interneurons in the model exhibit motif-spanning, high-activity regimes that mirror the dense inhibitory backdrop observed in HVC during singing. Figure 4 shows representative membrane potential traces for 20 TB interneurons, including both microcircuit-specific cells (light black) and non-microcircuit-specific cells (dark black). Across the motif, TB interneurons generate multiple bursts, consistent with their role as broadly recruited inhibitory controllers rather than segment-local, single-event units. These bursts arise from convergent AMPA excitation driven by distributed projection-neuron activity, inputs from HVC_{RA} neurons (from any microcircuit) and from both microcircuit-specific (MS) and non-microcircuit-specific (NMS) HVC_X neurons (as in Figure 2), so TB interneurons effectively integrate motif-wide excitation

and translate it into structured inhibitory epochs (quantified below; Figures 6-7). TB interneurons also show irregular spiking between (and outside) burst epochs due to stochastic synaptic pulse trains (Methods), capturing the synaptic "bombardment" regime characteristic of *in vivo* networks where ongoing fluctuations coexist with event-like structure[53–55]. In this circuit, burst epochs riding on an irregular inhibitory background provide robustness (ongoing inhibitory tone) without requiring interneurons to be silent outside assigned windows.

Critically, the model also shows that sequence propagation is highly sensitive to TB interneuron excitability, because TB output directly gates whether MS HVC_X neurons can escape inhibition to generate the rebound bursts that drive the $HVC_X \rightarrow HVC_{RA}$ relay, a pathway whose causal relevance is now strengthened by the new Trusel et al.[43] findings. When excitation from projection neurons onto MS TB interneurons becomes too strong ($\gg g_{AMPA}$), TB cells enter regimes of dense, near-continuous bursting/spiking, imposing prolonged inhibition onto MS X-projecters; this delays or halts rebound and thereby destabilizes (or stops) propagation. Similarly, perturbing intrinsic rebound-supporting conductances in MS TB interneurons can push them into runaway excitation: increasing g_{CaT} (3-fold) or g_H (5-fold) in INT_{TB}^{i} drives sustained TB activation that continuously inhibits X_{SSS}^{i}, preventing rebound and blocking transmission to $HVC_{RA_1}^{i+1}$, thereby halting the sequence (Supplementary Figure 3A-B). Mechanistically, these perturbations are particularly destabilizing because both channel types are powerful excitability controllers near rest: T-type Ca^{2+} channels open close to resting membrane potential and markedly enhance responsiveness when upregulated, while H-channels strongly shape baseline depolarizing drive and excitability (and can indirectly promote calcium entry by

maintaining depolarized regimes). Thus, TB burst count, duration, and spikes-per-burst are not merely descriptive outputs, they are emergent consequences of synaptic drive and intrinsic excitability that must remain within a constrained regime to preserve inhibitory timing, enable HVC_X rebound, and maintain stable motif-scale propagation.

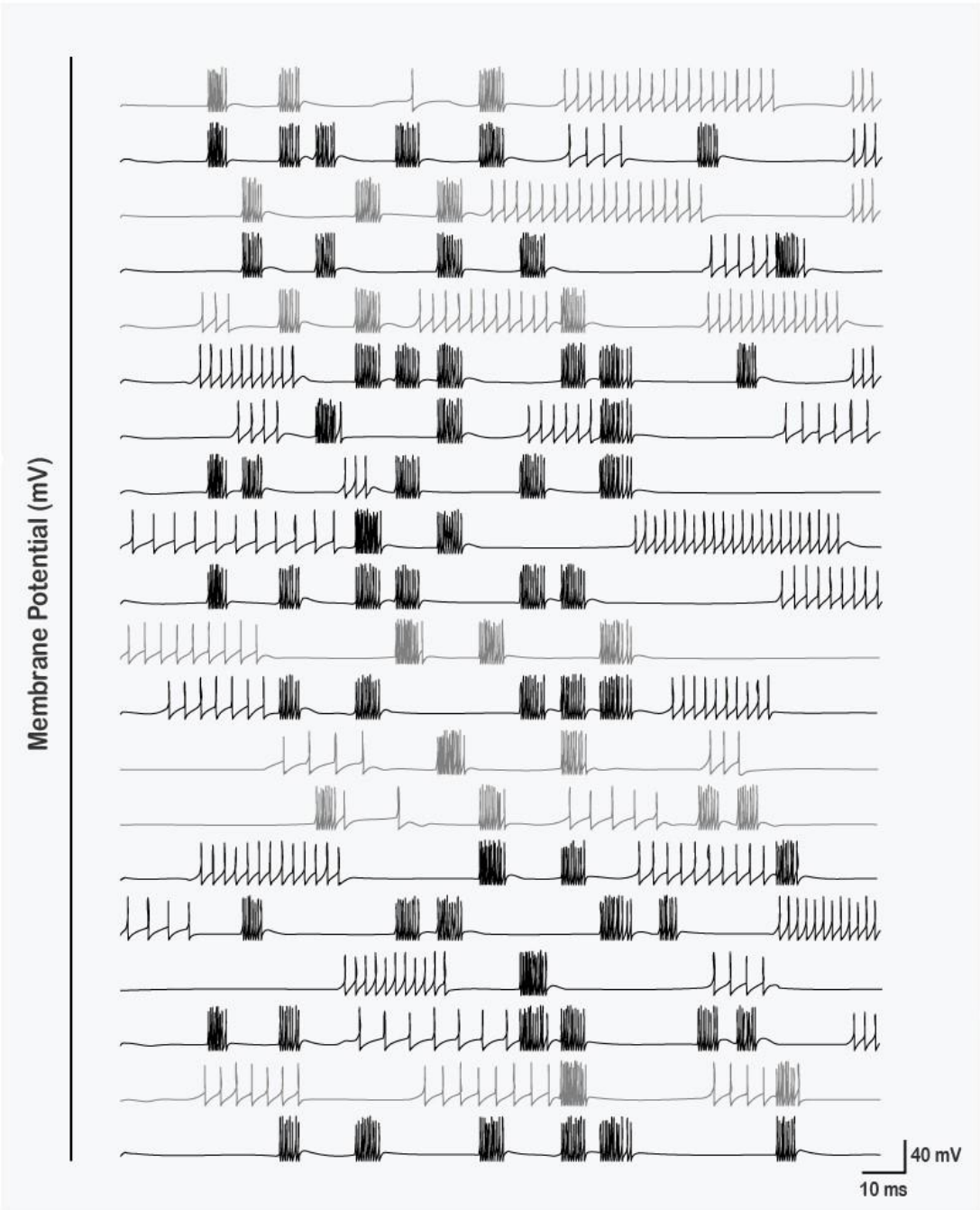

Figure 4. Motif-spanning bursting and irregular spiking in tonic HVC interneurons. Representative membrane potential traces from 20 tonic-bursting (TB) interneurons during a simulated motif, including microcircuit-specific cells (light gray) and non-microcircuit-specific cells (black). TB interneurons generate multiple bursts distributed across the motif, driven by convergent excitation from HVC_{RA} neurons (across microcircuits) and from both MS and NMS HVC_X neurons (Figure 2). Inter-burst irregular spiking arises from stochastic synaptic pulse trains (Methods), producing an *in vivo*-like inhibitory activity.

Activity patterns of HVC_X neurons

HVC_X neurons generate 2-4 motif-locked bursts in the model (Figure 5; 20 cells shown), for both MS (light blue) and NMS (dark blue) populations, matching the core *in vivo* phenomenology of HVC_X during singing[19,22,26,27]. Mechanistically, HVC_X bursts are post-inhibitory rebound events: MS HVC_X neurons are inhibited primarily by their assigned MS tonic-bursting interneuron, whereas NMS HVC_X neurons can be inhibited by multiple interneurons, naturally producing heterogeneity in burst count and spikes-per-burst. This rebound mechanism provides a principled route for inhibition to create precisely timed excitation via deinactivation of T-type Ca^{2+} channels and recruitment of I_h [47–49]. In HVC, this logic is especially consequential because rebound-generated HVC_X bursts can be converted directly into forward progression through the $HVC_X \rightarrow HVC_{RA}$ relay, now reinforced by recent connectivity mapping[43]: inhibition becomes a timing signal that launches the next segment rather than a merely destabilizing brake.

Because the projection from X_{SSS}^{i} to $HVC_{RA_1}^{i+1}$ is the model's critical relay for advancing from one sub-syllabic segment to the next (Figures 2 and 6), it is also a natural point of fragility. In the model, each rebound burst in X_{SSS}^{i} must be strong enough to drive $HVC_{RA_1}^{i+1}$ suprathreshold; otherwise, the next microcircuit is not recruited and propagation collapses at the boundary. Supplementary Figure 4 illustrates a synaptic route to relay failure: reducing the GABAergic conductance from the MS tonic interneuron to the MS X-

projecter (g_{GABA}, $INT_{TB}^{i} \rightarrow X_{SSS}^{i}$) by 10-fold preserves the burst in INT_{TB}^{i} (still driven by the terminal RA neuron $HVC_{RA_6}^{i}$) and produces a visible sag in X_{SSS}^{i}, but release yields only a small rebound overshoot rather than a rebound burst. Consequently, X_{SSS}^{i} fails to recruit $HVC_{RA_1}^{i+1}$, later microcircuits remain silent (e.g., $HVC_{RA_3}^{j}$ and $HVC_{RA_5}^{k}$), INT_{TB}^{i} expresses only the single burst tied to microcircuit i (no later excitatory events arrive), and downstream phasic interneurons (e.g. INT_{PB}^{j} and INT_{PB}^{k}) are silent because their local HVC_{RA} ensembles were never activated.

A second constraint is intrinsic: the relay is only as reliable as the ability of X_{SSS}^{i} to generate a suprathreshold rebound burst. Supplementary Figure 5A shows that reducing the T-type Ca^{2+} conductance (g_{CaT}) in X_{SSS}^{i} by 3-fold weakens/abolishes rebound bursting and collapses propagation with the same downstream signature as Supplementary Figure 4. Conversely, Supplementary Figure 5B shows that increasing the Ca^{2+}-dependent K^{+} conductance (g_{SK}) in X_{SSS}^{i} by 2-fold suppresses rebound excitability: the potentiated outward I_{SK} counteracts the inward rebound drive from I_{CaT} (with support from I_h), preventing X_{SSS}^{i} from reaching a burst-permissive regime and breaking the chain. Together, these perturbations define a bounded “rebound window” required for stable propagation, where inward rebound currents (dominated by g_{CaT}, supported by I_h) must overcome, but remain balanced by, activity-dependent outward stabilization (g_{SK}).

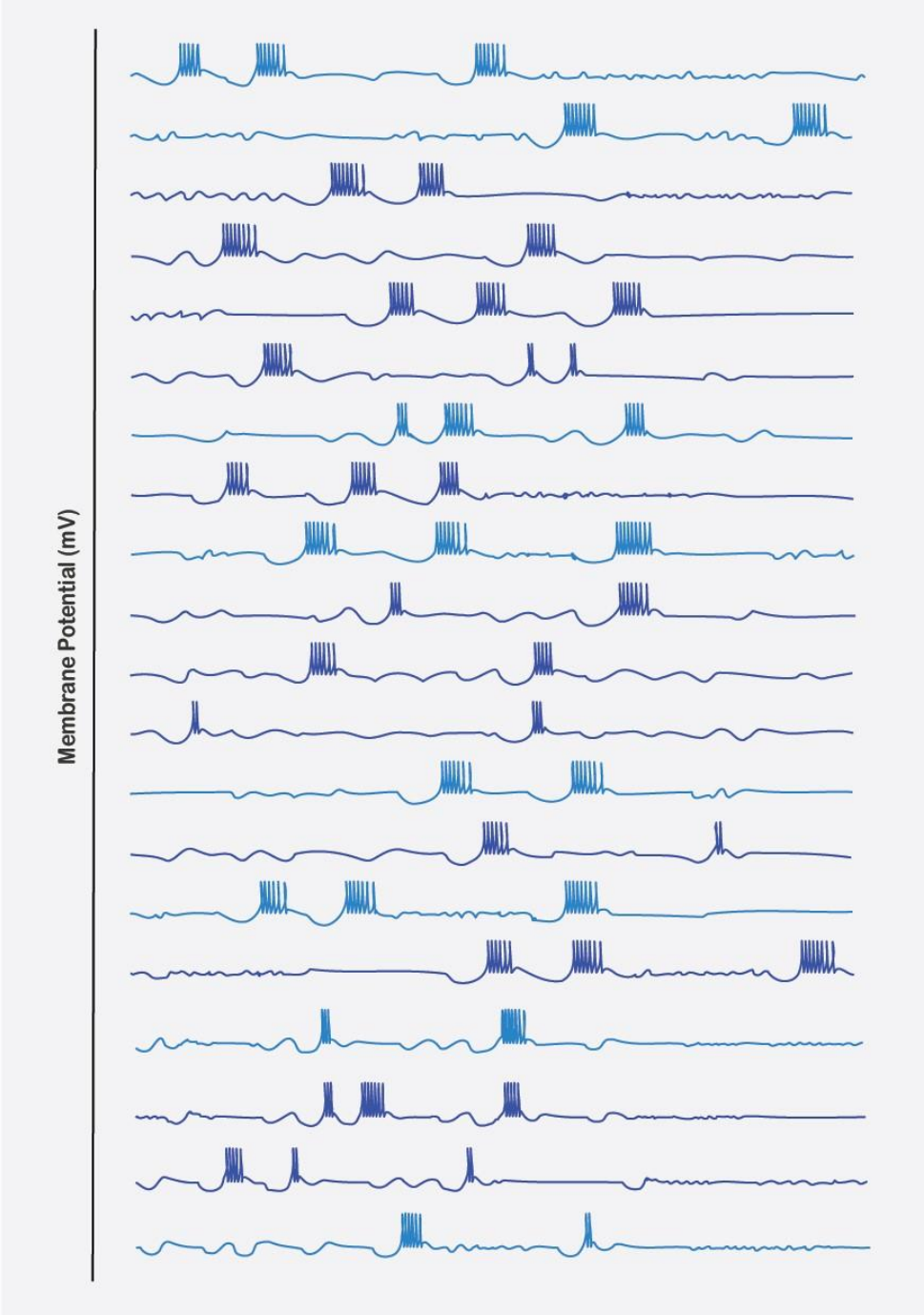

Figure 5. Rebound-driven multi-burst firing in HVC_X neurons. Representative membrane potential traces from 20 HVC_X neurons during a simulated motif, including microcircuit-specific (MS; light blue) and non-microcircuit-specific (NMS; dark blue) cells. HVC_X neurons generate 2-4 bursts with cell-to-cell variability in burst count and spikes per burst. In the model, bursts arise as post-inhibitory rebounds: MS HVC_X neurons are inhibited primarily by their assigned microcircuit-specific tonic-bursting interneuron, whereas NMS HVC_X neurons can be inhibited by multiple interneurons from the global pool. These rebound bursts provide a motif-scale timing signal that supports sequence propagation and aligns with experimentally observed multi-burst HVC_X firing.

Finally, the model identifies an opposite failure mode in which rebound gain becomes too large. Supplementary Figure 6 increases g_H in X_{SSS}^i by 5-fold, pushing X_{SSS}^i into runaway excitation: it fires nearly continuously, pausing only during inhibition from INT_{TB}^i. Through the $X_{SSS}^i \rightarrow HVC_{RA_1}^{i+1}$ projection, this immediately drives $HVC_{RA_1}^{i+1}$ into continuous firing - pathological for HVC$_{RA}$ - and the effect propagates through microcircuit $i+1$, causing the remaining HVC$_{RA}$ neurons to adopt similarly dense firing. This forces INT_{TB}^{i+1} into high-frequency firing and strongly clamps X_{SSS}^i for most of the motif. Notably, INT_{TB}^{i+1} becomes silent only during the same brief window when X_{SSS}^i is silenced by INT_{TB}^i; during that shared silent window X_{SSS}^{i+1} escapes inhibition and generates a single rebound burst that eventually activates $HVC_{RA_1}^{i+2}$, but at a markedly delayed time outside its intended SSS. Thus, excessive I_h need not simply "break" the chain, it can time-warp it, producing dense firing in HVC$_{RA}$ (instead of ultra-sparse bursts), high-frequency firing in HVC$_X$ (instead of 2-4 rebounds), delayed recruitment of downstream microcircuits (phase shifts), and in other parameter regimes complete sequence failure.

Neuronal interplays within the microcircuit

We next dissect the tonic-phasic division of labor at the single-microcircuit level. In the example microcircuit i (Figure 6), the tonic interneuron INT_{TB}^i receives AMPA drive from the terminal HVC$_{RA}$ neuron of microcircuit i ($HVC_{RA_6}^i$ (top red; the segment-completion signal; Figures 2-3) and additional HVC$_{RA}$ neurons activated later in the motif. As a result, INT_{TB}^i emits multiple time-locked bursts and shows irregular inter-burst spiking due to ongoing synaptic drive (Methods). Each INT_{TB}^i burst inhibits the MS HVC$_X$ neuron X_{SSS}^i, and release recruits a post-inhibitory rebound burst. The first rebound burst excites the

next microcircuit's chain-initiating HVCRA neuron $HVC_{RA_1}^{i+1}$ to launch the subsequent HVCRA packet and advance the sequence. Later INT_{TB}^{i} - driven rebound bursts would, in principle, re-excite $HVC_{RA_1}^{i+1}$; these off-time restarts are prevented by the phasic interneurons active in the current segment ($INT_{TB}^{j}/INT_{TB}^{k}$), which veto HVCRA spiking outside its assigned window (see Figure 2).

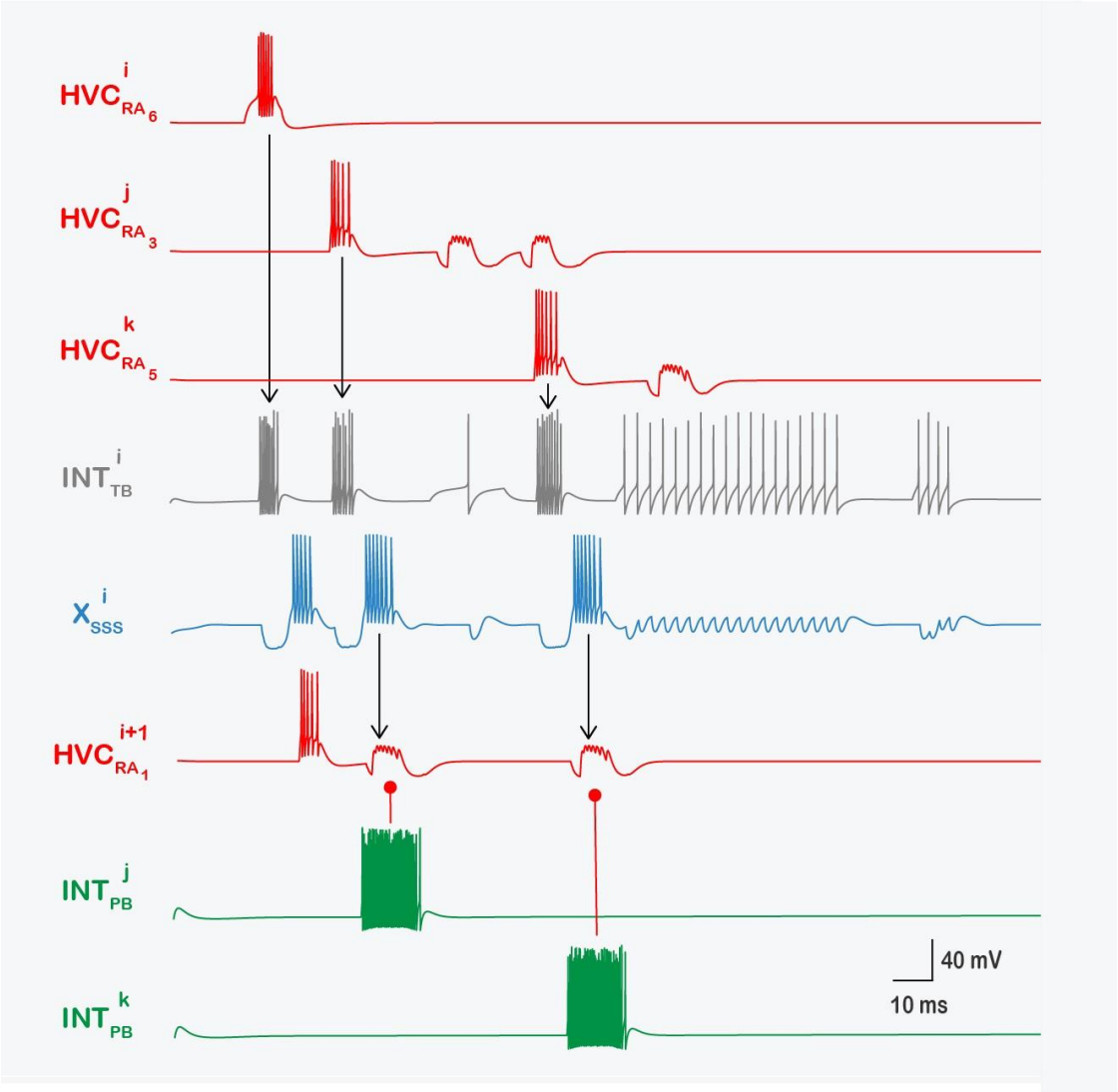

Figure 6. Microcircuit interplay: tonic inhibition recruits HVC_X rebound bursts for propagation, while phasic inhibition vetoes off-time HVC_{RA} reactivation. Representative membrane potential traces showing stabilizing interactions within and across microcircuits. Three HVC_{RA} neurons ($HVC^i_{RA_6}$, $HVC^j_{RA_3}$, $HVC^k_{RA_5}$; **red**) provide AMPA excitation to the microcircuit-specific tonic interneuron INT^i_{TB} (**gray**), eliciting time-locked bursts that inhibit the microcircuit-specific HVC_X neuron X^i_{SSS} (**blue**) and generate post-inhibitory rebound bursts. The first rebound excites the next microcircuit's chain-initiating neuron $HVC^{i+1}_{RA_1}$ (red) to trigger correct propagation, whereas later rebounds would re-excite $HVC^{i+1}_{RA_1}$ and induce non-biological extra HVC_{RA} bursts. Segment-specific phasic interneurons (INT^j_{PB}, INT^k_{PB}; **green**) prevent these restarts via GABAergic inhibition onto $HVC^{i+1}_{RA_1}$, converting would-be spikes into subthreshold "bumps."

Phasic-veto failure modes define a narrow operational regime. Weakening PB → HVC_{RA} inhibition undermines this stabilizing veto and allows ectopic HVC_{RA} bursts to escape. When g_{GABA} from a single phasic burster (e.g. INT^k_{PB}) to its HVC_{RA} targets is reduced 5-fold (Supplementary Figure 7A), an off-time rebound-driven event that should be vetoed instead produces an ectopic burst in $HVC^{i+1}_{RA_1}$, which then seeds downstream off-schedule activity through interneuron/X-projecter interactions. When PB → HVC_{RA} inhibition is reduced 5-fold globally across phasic bursters (Supplementary Figure 7B), the failure becomes circuit-wide: the network loses segment exclusivity, many HVC_{RA} neurons drift into inappropriate multi-burst/tonic-like regimes, and activity becomes re-entrant and non-song-like. Conversely, the model shows that PB neurons must also avoid excessive intrinsic excitability: increasing g_{CaT} 4-fold or g_H 5-fold in a representative phasic burster INT^j_{PB} (Supplementary Figure 8A-B) converts a brief, segment-locked veto into a persistently active inhibitor, imposing an effectively continuous clamp on its postsynaptic HVC_{RA} targets and locally abolishing legitimate segment bursts. Thus, stable propagation requires PB interneurons to remain within a constrained regime: strong enough to veto off-time reactivation, but not so excitable that they extinguish the sparse, segment-locked HVC_{RA} code they are meant to protect.

Tonicity in the bursting activity of HVC$_{INT}$ neurons

Figure 7 shows how tonic-bursting interneurons (INT_{TB}) acquire motif-spanning "tonicity" through distributed convergent excitation. We highlight one representative interneuron from the non-microcircuit-specific (NMS) pool, INT_{TB}^{12}, alongside the activity of all presynaptic projection neurons that contact it. In this example, INT_{TB}^{12} receives random AMPAergic inputs from three HVC$_{RA}$ neurons ($HVC_{RA_3}^{m}$, $HVC_{RA_1}^{n}$, $HVC_{RA_1}^{o}$) and four HVC$_X$ neurons: one microcircuit-specific projector (X_{SSS}^{i}) and three NMS X-projectors (HVC_X^4, HVC_X^6, HVC_X^{11}). This convergence recruits multiple interneuron bursts distributed across the motif.

More generally, in the model the number of INT_{TB} bursts are set by the burst "opportunities" provided by presynaptic partners: each presynaptic HVC$_{RA}$ or HVC$_X$ burst can recruit a time-locked interneuron burst. The strength of each interneuron burst (spike count/firing frequency) is governed primarily by the effective AMPA conductance from projection neurons onto INT_{TB}, such that stronger coupling produces more powerful bursts. The model further predicts a nonlinear summation regime: temporally overlapping presynaptic bursts drive disproportionately strong interneuron responses. This is illustrated by the asterisk in Figure 7, where coincident bursts in $HVC_{RA_1}^{o}$, HVC_X^6 and HVC_X^{11} yield a markedly stronger, denser burst in INT_{TB}^{12}. In the next section, we show that intrinsic conductances controlling interneuron excitability can further reshape recruitment and, when perturbed, destabilize sequence propagation.

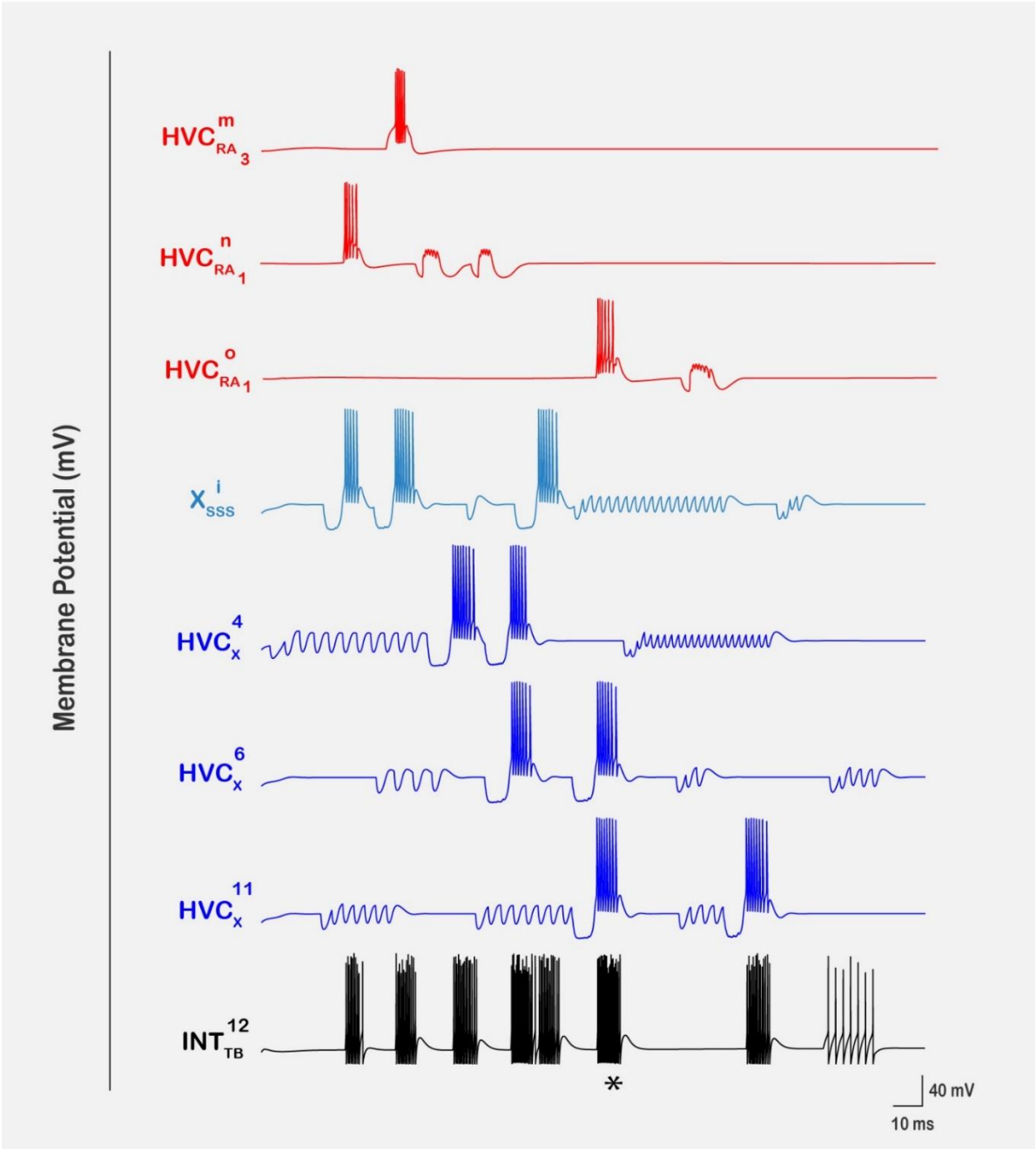

Figure 7. Distributed convergence from HVC$_{RA}$ and HVC$_X$ drives tonic bursting in HVC interneurons. Representative membrane potential traces illustrating how a tonic-bursting interneuron from the non-microcircuit-specific pool, INT_{TB}^{12} (black), is recruited by convergent excitation from both classes of projection neurons. INT_{TB}^{12} receives AMPAergic inputs from three HVC$_{RA}$ neurons ($HVC_{RA_3}^{m}$, $HVC_{RA_1}^{n}$, $HVC_{RA_1}^{o}$; red) and from four HVC$_X$ neurons, including one microcircuit-specific X-projector (X_{SSS}^{i}; light blue) and three non-microcircuit-specific X-projectors (HVC_X^4, HVC_X^6, HVC_X^{11}; dark blue). Each presynaptic burst can recruit a time-locked burst in INT_{TB}^{12}, yielding motif-spanning multi-burst activity. The asterisk marks a particularly strong interneuron burst produced by near-coincident presynaptic bursting (here $HVC_{RA_1}^{o}$, HVC_X^6 and HVC_X^{11}), illustrating temporal summation of excitatory drive that increases interneuron firing frequency and spike count.

Rebound bursting in HVC$_X$ neurons

HVC$_X$ bursting in the model is governed by a tight coupling between synaptic and intrinsic mechanisms, which together set both how many rebound bursts occur and how strong each burst becomes. Synaptically, rebound amplitude scales with the depth, duration, and synchrony of inhibition: larger GABA$_A$ conductances, greater temporal overlap among inhibitory interneuron bursts, and longer/denser inhibitory epochs all potentiate rebound, converting release from inhibition into either a weak depolarization or a full high-frequency burst. Thus, inhibition does not merely silence HVC$_X$, it sets the initial conditions for the rebound event. Intrinsically, rebound is amplified primarily by T-type Ca^{2+} current and I_h , which are progressively recruited by hyperpolarization (via deinactivation/activation) and then provide inward drive at release. Burst spike count is constrained by an opposing stabilizer, g_{SK}, which dampens excitability and limits spikes-per-burst. Together, HVC$_X$ bursts emerge from a push-pull interaction: inhibition-recruited inward currents (I_{CaT}, I_h) versus activity-dependent outward stabilization (I_{SK}).

Figure 8A illustrates these dynamics for an exemplar NMS X-projecting neuron, HVC_X^{14}, inhibited by three tonic interneurons (INT_{TB}^{j}, INT_{TB}^{5}, INT_{TB}^{16}). Periods of hyperpolarizing "sags" coincide with interneuron bursting and are summarized by bars (orange: strong/high-frequency inhibition; pink: weaker/sparser inhibition). Because inhibitory events often arrive in successive or overlapping bursts, HVC_X^{14} frequently remains trapped below threshold; brief gaps between inhibitory epochs yield only small rebound depolarizations, implying the release window is too short for I_{CaT} and I_h to fully engage. By contrast, two longer release intervals follow sufficiently strong/overlapping inhibition and allow I_{CaT} + I_h to reach burst-permissive states, producing robust rebound bursts,

with g_{SK} shaping burst termination and spike count. Functionally, this inhibition-to-rebound transform is attractive for sequence generation because it allows inhibitory networks to act as *event setters*: the circuit can encode "when" a burst should occur by controlling the depth, duration, and synchrony of inhibition, rather than relying solely on excitatory ramping.

Parallel "burst manifolds" in HVC_X emerge naturally from the microcircuit chain. Recent reanalysis indicates that HVC_X bursts can organize into multiple motif-spanning sequences ("parallel lines"), suggesting structured time coding in HVC_X alongside HVC_{RA}'s ultra-sparse code[27]. To compare directly, we constructed the same "neuron cascade" (Figure 8B): bursts from each HVC_X neuron are plotted on one row; neurons are sorted by first-burst time; first bursts are blue and later bursts red; each marker indicates the first spike time of that burst.

Applied to microcircuit-specific HVC_X neurons, the model reproduces the key signature: first bursts form a quasi-linear manifold spanning the motif, and later bursts form additional quasi-linear manifolds approximately parallel to the first. This structure is emergent, not imposed by alignment rules, and matches the qualitative organization reported *in vivo*[27]. We focus on microcircuit-specific HVC_X neurons because the architecture supplies a mechanistic explanation: their rebound timing is organized by repeated, stereotyped inhibitory scheduling within the microcircuit chain. NMS HVC_X neurons can generate bursts that sometimes fall near these manifolds, but because their inhibitory drive is random (PB/TB inputs from the global pool), the model does not assign a unique functional origin to that alignment.

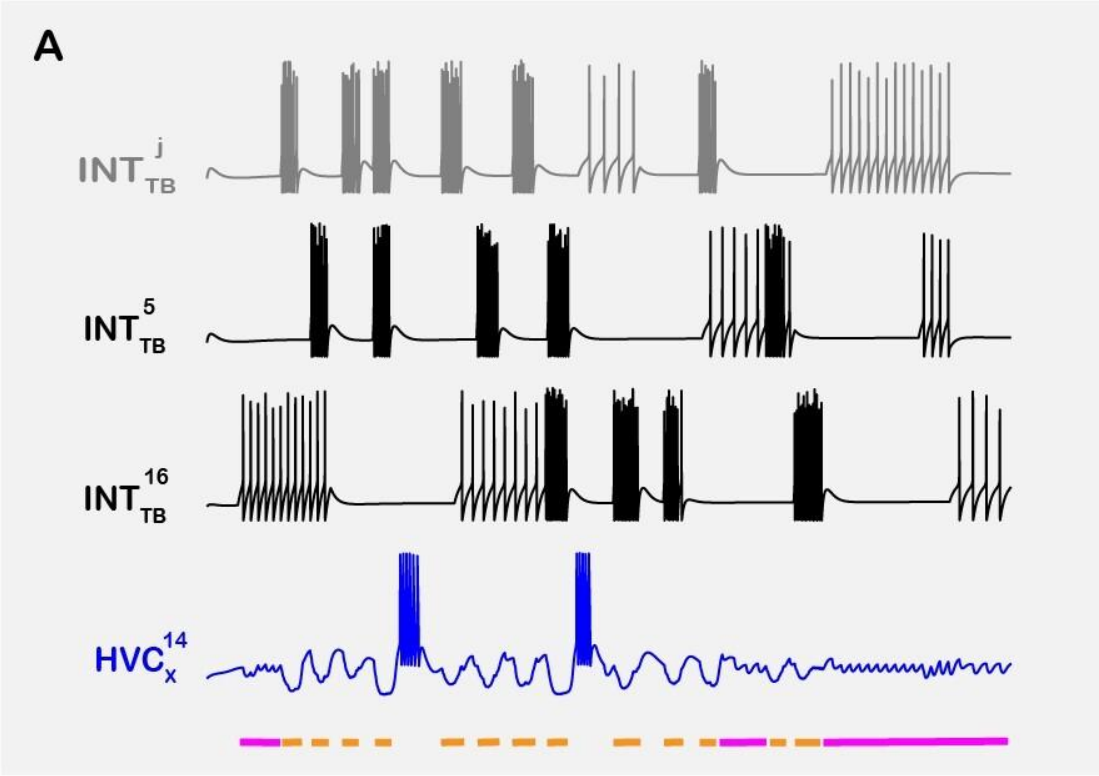
A
INT$^{j}_{TB}$
INT$^{5}_{TB}$
INT$^{16}_{TB}$
HVC$^{14}_{X}$

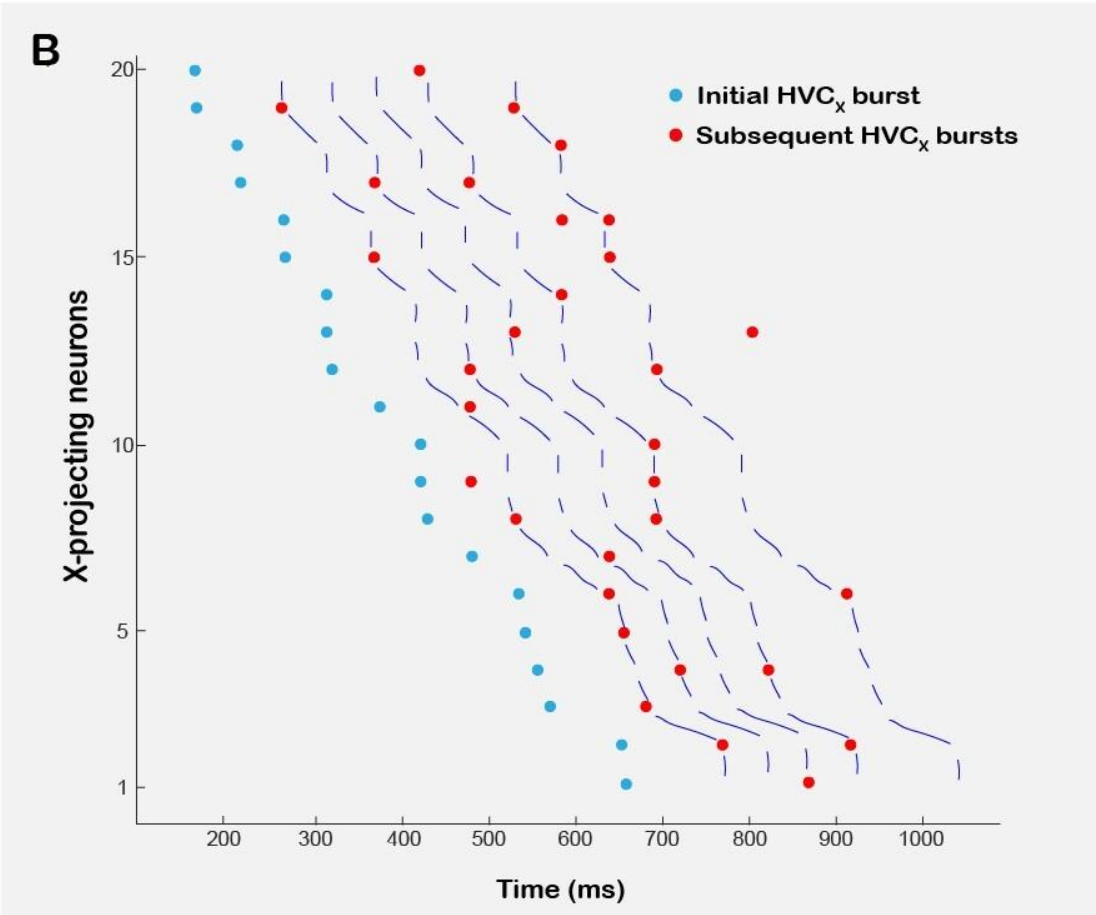
B
Initial HVC$_X$ burst
Subsequent HVC$_X$ bursts
X-projecting neurons
Time (ms)
20
15
10
5
1
200
300
400
500
600
700
800
900
1000

Figure 8. Inhibition-sculpted rebound bursting generates motif-locked HVC$_X$ activity and parallel burst manifolds. (**A**). Example non-microcircuit-specific X-projecting neuron (HVC_X^{14}, blue) illustrating post-inhibitory rebound bursting driven by convergent inhibition from three tonic-bursting interneurons (INT_{TB}^{j}, INT_{TB}^{5}, INT_{TB}^{16}; gray/black). Periods of interneuron bursting produce hyperpolarizing sags in HVC_X^{14} and suppress spiking; release from inhibition yields rebound depolarizations and occasional rebound bursts. Colored bars beneath the HVC_X^{14} trace indicate epochs of inhibition: **orange** denotes strong inhibition associated with high-frequency interneuron bursting, whereas **pink** denotes weaker inhibition associated with sparse interneuron firing. Only sufficiently strong/prolonged inhibition followed by a sufficiently long silent interval permits a full rebound burst, consistent with rebound recruitment by intrinsic currents (e.g., I_{CaT}, I_h). (**B**) "Neuron cascade" representation of bursting in microcircuit-specific HVC$_X$ neurons (X_{SSS}) aligned to the canonical motif time base. Each row corresponds to a single neuron; neurons are ordered by the time of their first burst. Each marker denotes the time of the first spike in a burst: **blue** circles indicate the initial burst for each neuron and **red** circles indicate subsequent bursts. Initial bursts form a quasi-linear manifold across neurons, and later bursts form additional quasi-linear manifolds that run approximately parallel, recapitulating the "parallel lines" of HVC$_X$ bursting reported experimentally (Fetterman & Margoliash, 2023). Lines illustrate the trajectory of bursts across successive events for each neuron, highlighting motif-spanning organization of multiple HVC$_X$ burst sequences.

Supplementary Figure 9 provides a schematic account of how parallel manifolds arise. In brief, offsets between first bursts of successive X_{SSS} neurons reflect the propagation time through each microcircuit (set by SSS duration and HVC$_{RA}$ chain length), while later bursts are produced by additional INT_{TB} - driven inhibitory events that recur at reproducible motif phases. This combination - segment timing plus repeated inhibitory scheduling - naturally generates parallel, shifted "passes" of rebound bursting and yields testable predictions for how manipulations that stretch/compress SSS duration or alter INT_{TB} recruitment should reshape manifold spacing.

Discussion

We developed a biophysically grounded network model of zebra finch HVC that resolves a long-standing mechanistic tension: how ultra-sparse, single-burst HVC_{RA} activity can coexist with multi-burst HVC_X firing while still propagating a motif-precise sequence. The key solution is to treat inhibition as an active timing resource. Tonic interneuron bursts schedule post-inhibitory rebound in HVC_X, and the resulting $HVC_X \rightarrow HVC_{RA}$ excitation provides a forward trigger at each segment boundary, while phasic inhibition defines segment-specific windows that veto off-time reactivation and preserve the "one-time-only" HVC_{RA} code.

This framework is strengthened by recent synaptic mapping in HVC indicating robust monosynaptic $HVC_X \rightarrow HVC_{RA}$ excitation and demonstrating that brief intra-HVC excitation can evoke restart-like motifs[56]. In our model, the same relay that enables reliable forward progression is also the natural locus of fragility: if rebound output is weakened (e.g., reduced inhibition onto X_{SSS}, reduced g_{CaT}, or elevated g_{SK}), propagation fails; if rebound gain is pushed too high (e.g., excessive I_h), the circuit transitions toward pathological dense firing and timing drift. Thus, stability emerges from a bounded rebound regime, not wiring alone.

Conceptually, the model unifies motifs that recur across timing circuits, release-from-inhibition generating precisely timed events and inhibitory windowing enforcing exclusivity, but ties them to identified HVC cell types and conductances. This cell-type grounding also provides an interpretable account of higher-order population structure: repeated inhibitory scheduling produces multiple motif-spanning "passes" of HVC_X

rebound bursting, yielding parallel burst manifolds reminiscent of recent reanalysis of HVC_X activity[27].

The model makes concrete, testable predictions. Increasing AMPA strength along HVC_{RA} chains or across the $HVC_X \rightarrow HVC_{RA}$ relay should advance recruitment and increase HVC_{RA} spike count, whereas elevating g_A should delay or veto HVC_{RA} recruitment within a segment. Manipulations that enhance I_{CaT}/I_h in HVC_X neurons should increase rebound probability and burst strength, while increasing g_{SK} (or reducing Ca^{2+} entry) should truncate bursts and can break propagation at segment boundaries. Finally, weakening $PB \rightarrow HVC_{RA}$ inhibition should selectively permit off-window HVC_{RA} bursts and induce localized timing errors, whereas excessive PB excitability should over-clamp HVC_{RA} targets and abolish legitimate segment activity.

Several extensions remain. The present work focuses on mechanism rather than learning; incorporating plasticity rules that tune synaptic gains and intrinsic conductances could connect the rebound, veto architecture to how birds acquire and adapt song. Future work should also integrate interactions with upstream/downstream structures (e.g., NIf/Uva inputs and the basal ganglia loop), and explore how heterogeneity across interneuron subtypes and non-microcircuit-specific populations modulates robustness. More broadly, the model illustrates how conserved cellular mechanisms - post-inhibitory rebound and precisely timed inhibition - can be assembled into modular microcircuits that generate learned sequential behavior, offering testable predictions for how HVC implements millisecond-precise control in birdsong and, potentially, how analogous mechanisms support sequential computation in other vertebrate motor and cognitive systems.

References

1. Skaggs, W.E., McNaughton, B.L., Wilson, M.A., and Barnes, C.A. (1996). Theta phase precession in hippocampal neuronal populations and the compression of temporal sequences. Hippocampus *6*, 149–172. https://doi.org/10.1002/(SICI)1098-1063(1996)6:2%253C149::AID-HIPO6%253E3.0.CO;2-K.

2. Pastalkova, E., Itskov, V., Amarasingham, A., and Buzsáki, G. (2008). Internally generated cell assembly sequences in the rat hippocampus. Science *321*, 1322–1327. https://doi.org/10.1126/science.1159775.

3. MacDonald, C.J., Lepage, K.Q., Eden, U.T., and Eichenbaum, H. (2011). Hippocampal “time cells” bridge the gap in memory for discontiguous events. Neuron *71*, 737–749. https://doi.org/10.1016/j.neuron.2011.07.012.

4. Harvey, C.D., Coen, P., and Tank, D.W. (2012). Choice-specific sequences in parietal cortex during a virtual-navigation decision task. Nature *484*, 62–68. https://doi.org/10.1038/nature10918.

5. Buzsáki, G., and Tingley, D. (2018). Space and Time: The Hippocampus as a Sequence Generator. Trends Cogn Sci *22*, 853–869. https://doi.org/10.1016/j.tics.2018.07.006.

6. Peters, A.J., Chen, S.X., and Komiyama, T. (2014). Emergence of reproducible spatiotemporal activity during motor learning. Nature *510*, 263–267. https://doi.org/10.1038/nature13235.

7. Bou Diab, Z., Chammas, M., and Daou, A. (2025). Biophysical network modeling of temporal and stereotyped sequence propagation of neural activity in the premotor nucleus HVC. Elife *14*. https://doi.org/10.7554/eLife.105526.

8. Reiner, A., Laverghetta, A.V., Meade, C.A., Cuthbertson, S.L., and Bottjer, S.W. (2004). An immunohistochemical and pathway tracing study of the striatopallidal organization of area X in the male zebra finch. J Comp Neurol *469*, 239–261. https://doi.org/10.1002/cne.11012.

9. Fee, M.S., and Scharff, C. (2010). The songbird as a model for the generation and learning of complex sequential behaviors. ILAR J *51*, 362–377. https://doi.org/10.1093/ilar.51.4.362.

10. Vu, E.T., Mazurek, M.E., and Kuo, Y.C. (1994). Identification of a forebrain motor programming network for the learned song of zebra finches. J Neurosci *14*, 6924–6934. https://doi.org/10.1523/JNEUROSCI.14-11-06924.1994.

11. Yu, A.C., and Margoliash, D. (1996). Temporal hierarchical control of singing in birds. Science *273*, 1871–1875. https://doi.org/10.1126/science.273.5283.1871.

12. Fee, M.S., Kozhevnikov, A.A., and Hahnloser, R.H.R. (2004). Neural mechanisms of vocal sequence generation in the songbird. Ann N Y Acad Sci *1016*, 153–170. https://doi.org/10.1196/annals.1298.022.

13. Long, M.A., and Fee, M.S. (2008). Using temperature to analyse temporal dynamics in the songbird motor pathway. Nature *456*, 189–194. https://doi.org/10.1038/nature07448.

14. Mooney, R. (2009). Neurobiology of song learning. Curr Opin Neurobiol *19*, 654–660. https://doi.org/10.1016/j.conb.2009.10.004.

15. Fee, M.S., and Goldberg, J.H. (2011). A hypothesis for basal ganglia-dependent reinforcement learning in the songbird. Neuroscience *198*, 152–170. https://doi.org/10.1016/j.neuroscience.2011.09.069.

16. Vicario, D.S. (1991). Neural mechanisms of vocal production in songbirds. Curr Opin Neurobiol *1*, 595–600. https://doi.org/10.1016/s0959-4388(05)80034-0.

17. Bolhuis, J.J., Okanoya, K., and Scharff, C. (2010). Twitter evolution: converging mechanisms in birdsong and human speech. Nat Rev Neurosci *11*, 747–759. https://doi.org/10.1038/nrn2931.

18. Hahnloser, R.H.R., Kozhevnikov, A.A., and Fee, M.S. (2002). An ultra-sparse code underlies the generation of neural sequences in a songbird. Nature *419*, 65–70. https://doi.org/10.1038/nature00974.

19. Kozhevnikov, A.A., and Fee, M.S. (2007). Singing-related activity of identified HVC neurons in the zebra finch. J Neurophysiol *97*, 4271–4283. https://doi.org/10.1152/jn.00952.2006.

20. Fujimoto, H., Hasegawa, T., and Watanabe, D. (2011). Neural coding of syntactic structure in learned vocalizations in the songbird. J Neurosci *31*, 10023–10033. https://doi.org/10.1523/JNEUROSCI.1606-11.2011.

21. Long, M.A., Jin, D.Z., and Fee, M.S. (2010). Support for a synaptic chain model of neuronal sequence generation. Nature *468*, 394–399. https://doi.org/10.1038/nature09514.

22. Amador, A., Perl, Y.S., Mindlin, G.B., and Margoliash, D. (2013). Elemental gesture dynamics are encoded by song premotor cortical neurons. Nature *495*, 59–64. https://doi.org/10.1038/nature11967.

23. Cannon, J., Kopell, N., Gardner, T., and Markowitz, J. (2015). Neural Sequence Generation Using Spatiotemporal Patterns of Inhibition. PLoS Comput Biol *11*, e1004581. https://doi.org/10.1371/journal.pcbi.1004581.

24. Kosche, G., Vallentin, D., and Long, M.A. (2015). Interplay of inhibition and excitation shapes a premotor neural sequence. J Neurosci *35*, 1217–1227. https://doi.org/10.1523/JNEUROSCI.4346-14.2015.

25. Markowitz, J.E., Liberti, W.A. 3rd, Guitchounts, G., Velho, T., Lois, C., and Gardner, T.J. (2015). Mesoscopic patterns of neural activity support songbird cortical sequences. PLoS Biol *13*, e1002158. https://doi.org/10.1371/journal.pbio.1002158.

26. Lynch, G.F., Okubo, T.S., Hanuschkin, A., Hahnloser, R.H.R., and Fee, M.S. (2016). Rhythmic Continuous-Time Coding in the Songbird Analog of Vocal Motor Cortex. Neuron *90*, 877–892. https://doi.org/10.1016/j.neuron.2016.04.021.

27. Fetterman, G.C., and Margoliash, D. (2023). Rhythmically bursting songbird vocomotor neurons are organized into multiple sequences, suggesting a network/intrinsic properties model encoding song and error, not time. Preprint, https://doi.org/10.1101/2023.01.23.525213 https://doi.org/10.1101/2023.01.23.525213.

28. Dutar, P., Vu, H.M., and Perkel, D.J. (1998). Multiple cell types distinguished by physiological, pharmacological, and anatomic properties in nucleus HVc of the adult zebra finch. J Neurophysiol *80*, 1828–1838. https://doi.org/10.1152/jn.1998.80.4.1828.

29. Kubota, M., and Taniguchi, I. (1998). Electrophysiological characteristics of classes of neuron in the HVc of the zebra finch. J Neurophysiol *80*, 914–923. https://doi.org/10.1152/jn.1998.80.2.914.

30. Mooney, R. (2000). Different subthreshold mechanisms underlie song selectivity in identified HVc neurons of the zebra finch. J Neurosci *20*, 5420–5436. https://doi.org/10.1523/JNEUROSCI.20-14-05420.2000.

31. Wild, J.M., Williams, M.N., Howie, G.J., and Mooney, R. (2005). Calcium-binding proteins define interneurons in HVC of the zebra finch (Taeniopygia guttata). J Comp Neurol *483*, 76–90. https://doi.org/10.1002/cne.20403.

32. Mooney, R., and Prather, J.F. (2005). The HVC microcircuit: the synaptic basis for interactions between song motor and vocal plasticity pathways. J Neurosci *25*, 1952–1964. https://doi.org/10.1523/JNEUROSCI.3726-04.2005.

33. Shea, S.D., Koch, H., Baleckaitis, D., Ramirez, J.-M., and Margoliash, D. (2010). Neuron-specific cholinergic modulation of a forebrain song control nucleus. J Neurophysiol *103*, 733–745. https://doi.org/10.1152/jn.00803.2009.

34. Daou, A., Ross, M.T., Johnson, F., Hyson, R.L., and Bertram, R. (2013). Electrophysiological characterization and computational models of HVC neurons in the zebra finch. J Neurophysiol *110*, 1227–1245. https://doi.org/10.1152/jn.00162.2013.

35. Drew, P.J., and Abbott, L.F. (2003). Model of song selectivity and sequence generation in area HVc of the songbird. J Neurophysiol *89*, 2697–2706. https://doi.org/10.1152/jn.00801.2002.

36. Jin, D.Z. (2009). Generating variable birdsong syllable sequences with branching chain networks in avian premotor nucleus HVC. Phys Rev E Stat Nonlin Soft Matter Phys *80*, 051902. https://doi.org/10.1103/PhysRevE.80.051902.

37. Gibb, L., Gentner, T.Q., and Abarbanel, H.D.I. (2009). Brain stem feedback in a computational model of birdsong sequencing. J Neurophysiol *102*, 1763–1778. https://doi.org/10.1152/jn.91154.2008.

38. Gibb, L., Gentner, T.Q., and Abarbanel, H.D.I. (2009). Inhibition and recurrent excitation in a computational model of sparse bursting in song nucleus HVC. J Neurophysiol *102*, 1748–1762. https://doi.org/10.1152/jn.00670.2007.

39. Hamaguchi, K., Tanaka, M., and Mooney, R. (2016). A Distributed Recurrent Network Contributes to Temporally Precise Vocalizations. Neuron *91*, 680–693. https://doi.org/10.1016/j.neuron.2016.06.019.

40. Galvis, D., Wu, W., Hyson, R.L., Johnson, F., and Bertram, R. (2018). Interhemispheric dominance switching in a neural network model for birdsong. J Neurophysiol *120*, 1186–1197. https://doi.org/10.1152/jn.00153.2018.

41. Egger, R., Tupikov, Y., Elmaleh, M., Katlowitz, K.A., Benezra, S.E., Picardo, M.A., Moll, F., Kornfeld, J., Jin, D.Z., and Long, M.A. (2020). Local Axonal Conduction Shapes the Spatiotemporal Properties of Neural Sequences. Cell *183*, 537-548.e12. https://doi.org/10.1016/j.cell.2020.09.019.

42. Elmaleh, M., Kranz, D., Asensio, A.C., Moll, F.W., and Long, M.A. (2021). Sleep replay reveals premotor circuit structure for a skilled behavior. Neuron *109*, 3851-3861.e4. https://doi.org/10.1016/j.neuron.2021.09.021.

43. Trusel, M., Zuo, J., Alam, D.H., Marks, E.S., Koch, T.M.I., Cao, J., Pancholi, H., Zhao, Z., Cooper, B.G., Zhang, W.-H., et al. (2026). Holistic motor control of zebra finch song syllable sequences. Nature. https://doi.org/10.1038/s41586-025-10069-z.

44. Kornfeld, J., Benezra, S.E., Narayanan, R.T., Svara, F., Egger, R., Oberlaender, M., Denk, W., and Long, M.A. (2017). EM connectomics reveals axonal target variation in a sequence-generating network. Elife *6*, e24364. https://doi.org/10.7554/eLife.24364.

45. Pouille, F., and Scanziani, M. (2001). Enforcement of temporal fidelity in pyramidal cells by somatic feed-forward inhibition. Science *293*, 1159–1163. https://doi.org/10.1126/science.1060342.

46. Isaacson, J.S., and Scanziani, M. (2011). How inhibition shapes cortical activity. Neuron *72*, 231–243. https://doi.org/10.1016/j.neuron.2011.09.027.

47. Llinás, R., and Jahnsen, H. (1982). Electrophysiology of mammalian thalamic neurones in vitro. Nature *297*, 406–408. https://doi.org/10.1038/297406a0.

48. Huguenard, J.R. (1996). Low-threshold calcium currents in central nervous system neurons. Annu Rev Physiol *58*, 329–348. https://doi.org/10.1146/annurev.ph.58.030196.001553.

49. McCormick, D.A., and Bal, T. (1997). Sleep and arousal: thalamocortical mechanisms. Annu Rev Neurosci *20*, 185–215. https://doi.org/10.1146/annurev.neuro.20.1.185.

50. Marder, E., and Bucher, D. (2001). Central pattern generators and the control of rhythmic movements. Curr Biol *11*, R986-996. https://doi.org/10.1016/s0960-9822(01)00581-4.

51. Grillner, S. (2006). Neuronal networks in motion from ion channels to behaviour. An R Acad Nac Med (Madr) *123*, 297–298.

52. Hahnloser, R.H.R., Kozhevnikov, A.A., and Fee, M.S. (2002). An ultra-sparse code underlies the generation of neural sequences in a songbird. Nature *419*, 65–70. https://doi.org/10.1038/nature00974.

53. Softky, W.R., and Koch, C. (1993). The highly irregular firing of cortical cells is inconsistent with temporal integration of random EPSPs. J Neurosci *13*, 334–350. https://doi.org/10.1523/JNEUROSCI.13-01-00334.1993.

54. Shadlen, M.N., and Newsome, W.T. (1998). The variable discharge of cortical neurons: implications for connectivity, computation, and information coding. J Neurosci *18*, 3870–3896. https://doi.org/10.1523/JNEUROSCI.18-10-03870.1998.

55. Destexhe, A., Rudolph, M., and Paré, D. (2003). The high-conductance state of neocortical neurons in vivo. Nat Rev Neurosci *4*, 739–751. https://doi.org/10.1038/nrn1198.

56. Trusel, M., Zhao, Z., Alam, D.H., Marks, E.S., Ikeda, M.Z., and Roberts, T.F. (2025). Synaptic connectivity of sensorimotor circuits for vocal imitation in the songbird. Elife *14*. https://doi.org/10.7554/eLife.104609.